Inorganic Chemistry

pubs.acs.org/IC

Article

Inverse Perovskite Oxysilicides and Oxygermanides as Candidates for Nontoxic Infrared Semiconductor and Their Chemical Bonding Nature

Naoki Ohashi,* David Mora-Fonz, Shigeki Otani, Takeshi Ohgaki, Masashi Miyakawa, and Alexander Shluger

Cite This: https://dx.doi.org/10.1021/acs.inorgchem.0c02897

ABSTRACT: We have synthesized inverse-perovskite-type oxysilicides and oxygermanides represented by R_3SiO and R_3GeO (R = Ca and Sr) and studied their characteristics in the search for nontoxic narrow band gap semiconductors. These compounds exhibit a sharp absorption edge around 0.9 eV and a luminescence peak in the same energy range. These results indicate that the obtained materials have a direct-band electronic structure, which was confirmed by hybrid DFT calculations. These materials, made from earth abundant and nontoxic elements and with a relatively light electron/hole effective mass, represent strong candidates for nontoxic optoelectronic devices in the infrared range.

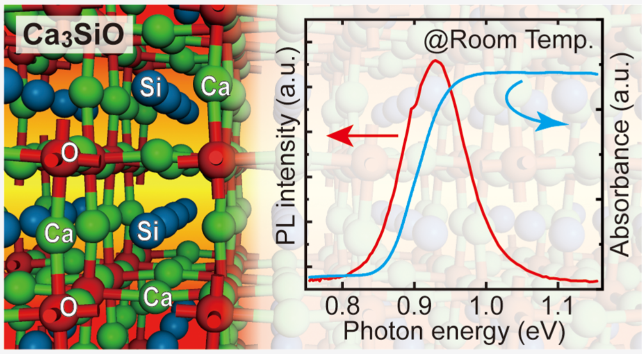

■ INTRODUCTION

Optoelectronic devices, particularly in the infrared (IR) range, have many important applications, such as sensors and emitters in optical fiber communication.[1,2] IR sensors are used, for example, in self-driving vehicles to achieve night time view.[3] However, most of the conventional semiconductors used in IR optics contain toxic elements, with the most typical example being mercury−cadmium−telluride (MCT).[4] Optical sensors utilizing MCT exhibit high sensitivity in the IR range, but all constituting elements, mercury (Hg),[5] cadmium (Cd),[6,7] and tellurium (Te),[8] are toxic and irreplaceable in the current semiconductor technology based on concepts used to develop II−VI and III−V semiconductors.

In particular, over several decades, the strategy for band gap (E_g) engineering in semiconductor development has been driven by elemental substitution in so-called II−VI or III−V systems.[9−12] This strategy is based on the observation that the band gap energy tends to be narrowed by adding elements with a large atomic number. The latter is one of the main reasons why MCTs have been adopted for optoelectronic devices used in IR ranges. Following this strategy, it is impossible to obtain narrow band gap materials without employing heavy elements in II−VI and III−V semiconductors. One of the directions to reduce the number of toxic elements used in those semiconductors is cation substitution. For instance, combining the I and III group elements for substitution of the group II elements, such as a combination of (Cu,Ga) and (Cu,In) for substitution of Cd, is one of the ways of toxicity reduction.[12−15] Toxic anions from the V and VI groups are, however, still necessary to form (I,III)−VI semiconductors. Hence, it is paramount to find appropriate *anions* to form compounds to overcome this limitation.

In this regard, silicides, germanides, and stannites, using group IV elements as a tetravalent *anion* in a formal charge state, have recently attracted interest in the search for nontoxic semiconductors. One such example is magnesium silicide (Mg_2Si),[16−21] which is formed by using silicon as a tetravalent anion. However, the Mg_2Si band structure is of indirect-transition-type and, hence, it cannot be useful as a light emitter.[22,23] In contrast, there are some silicide semiconductors with a direct-transition-type band structure, such as Sr_2Si and Ba_2Si,[24] but, to the best of our knowledge, their luminescence properties have not yet been reported. For applications in optoelectronics, particularly light emitting devices, it is essential to find semiconductors which exhibit the required luminescence properties.

Recently, the utilization of photonic structures has been proposed as a way to overcome the difficulty in fabricating nontoxic optoelectronic devices in the IR range. For instance, plasmonic structures composed of gold thin film have been

Received: September 29, 2020

used to enhance IR emission[25] and detection.[26] The efficiency of IR detection as high as characteristic to MCT-based devices has been achieved with GaAs-based devices combined with a photonic structure composed of gold. Other prospective R_3MO [R = (alkali earth elements) and M = (group IV elements)] compounds are attracting interest in terms of electron transport properties. Very recently, their thermoelectric properties have been studied in ref 27. Particularly, it has been reported that nonstoichiometric strontium stannite [$Sr_{3-x}SnO$ (R = Sr and M = Sn)] exhibits topological superconductivity.[28] These materials can become good candidates for nontoxic IR semiconductors with photonic structures for high efficiency devices in the IR range.

In this paper, we explore several new R_3MO compound semiconductors with a relatively narrow direct optical band gap. It has been reported that R_3MO compounds possess the inverse-perovskite-type crystal structure with corner-sharing [OR_6] octahedron units.[29−31] Formal charges of M, R, and O are expected to be $-4e$, $+2e$, and $-2e$, respectively. Because we are particularly interested in nontoxic materials with semiconducting properties, in this work, we focused on R_3MO compounds with relatively light elements, which include synthesis and characterization of oxysilicides and oxygermanides. The energy band structures of these compounds were calculated using hybrid density functional theory (h-DFT), and their optical properties were analyzed by optical absorption and luminescence spectroscopy. Our results confirm that these R_3MO materials have a direct-transition-type band structure and their band gap energy is less than 1 eV. Therefore, we suggest that the oxysilicides (Ca_3SiO, Sr_3SiO), oxygermanides (Ca_3GeO, Sr_3GeO), and their solid solutions are strong candidates for optoelectronic applications, including light emitters.

EXPERIMENTS

The inverse-perovskite-type R_3MO compounds, oxysilicides (M = Si) and oxygermanides (M = Ge) with R = Mg, Ca, and Sr and their solid solution compounds, were synthesized by solid-state reactions. Selected source materials were pure elemental compounds, such as Mg, Ca, Sr, Si, and Ge, and dioxides SiO_2 and GeO_2. Oxides were used as both the source of oxygen and M elements. The source materials were weighed to satisfy the atomic ratio of R:M:O = 3:1:1 and sealed in a tube made from pure metallic tantalum (Ta). The sealed precursors were heated in a pure Ar atmosphere at 900−1050 °C for 24−45 h to induce formation of R_3MO compounds. The reaction products were stored in a glass cylinder filled with liquid paraffin to prevent oxidation of the samples with air. The obtained samples were characterized by X-ray powder diffraction (XRD) for phase identification. The samples were covered with liquid paraffin to avoid oxidation during measurements.

Optical properties of the products were measured with a conventional UV−IR spectrometer at room temperature. Here, diffuse reflectance measurement was employed utilizing an integration sphere made of $BaSO_4$ for the pelletized samples formed by pressing. The luminescence properties of the samples were also measured at room temperature. A pulsed laser source (wavelength at 800 nm, repetition rate at 82 MHz, pulse width at 150 fs, and average power at about 50 mW) was used for excitation, whereas the luminescence spectra were obtained by an Acton VM-505 monochromator with a Hamamatsu G10899-03K InGaAs PIN photodiode detector. For photoluminescence (PL) measurements, the powder samples were fixed on conventional adhesive tape and pure nitrogen gas was flowed on the sample surface to prevent reaction between the sample and air. The absence of the luminescence peak from the adhesive tape was confirmed.

COMPUTATIONAL DETAILS

Electronic structure and lattice parameters of the R_3MO compounds were calculated using the periodic plane wave DFT code VASP (Vienna Ab initio Simulation Package)[32,33] with the projector-augmented wave (PAW) method[34,35] for describing interactions between the cores and the valence electrons (Ca:[10e], Si:[4e], Sr:[10e], Ge:[14e], Mg:[8e], and O:[6e]) of the involved atoms. The exchange-correlation energy was calculated using two generalized gradient approximation (GGA) functionals: Perdew−Burke−Ernzerhof (PBE)[36] and the PBE functional revised for solids, PBEsol.[37] For a more accurate description of electronic structure, the hybrid PBE0 and PBEsol0 functionals[38,39] were used with a 25% of the exact exchange.

Calculations were performed by assuming a *Pnma* symmetry (orthorhombic crystal system)[40] for every structure, in agreement with previous reports.[29,30] For the structural optimizations, total energy convergence to less than 1 meV/atom was achieved with respect to the **k**-point sampling and energy cutoff, keeping the symmetry fixed. A kinetic energy cutoff of 500 eV and a **k**-point spacing of 0.3 $Å^{-1}$ was used for bulk relaxations, whereas a single point calculation with a **k**-point spacing of 0.2 $Å^{-1}$ was used for the density of states (DOS). Structural optimization was achieved when the forces on the ions were all less than 0.01 eV $Å^{-1}$. The stability of the structure was studied by calculating the enthalpy of formation, which was done by comparing the total energy of the R_3MO structures and the compounds used as precursors during the synthesis. The obtained electronic structure was analyzed by calculating the projected density of state (PDOS) and local density of state (LDOS) using **k**-point sampling on the Monkhorst−Pack grid.[41,42] The energy-momentum dispersion of electrons (band diagram) was also calculated to evaluate electron and hole effective masses using the relationship

$$\frac{1}{m_{ij}^{*}} = \frac{\partial^2 E(\mathbf{k})}{\partial k_i \partial k_j} \frac{1}{\mathbf{h}^2} \qquad (1)$$

where $E(\mathbf{k})$ is defined as the eigenvalue of the band at a specific **k**-point, k_i and k_j are the ith and jth elements of **k**, and m_{ij}^{*} is the element of effective mass tensor. The band structure diagrams were plotted using the sumo package.[43] Moreover, the charge distribution in R_3MO was quantified using the Bader analysis.[44]

As mentioned, we focus on the exploration of different anions. In an attempt to provide a better characterization of the M^{4-} *anions*, we have considered not only R_3MO but also R_2M compounds. For consistency, both R_3MO and R_2M compounds were modeled using the VASP code with the nonlocal PBEsol0 functional. We note that, although there are several prior computational studies of R_2M compounds,[45−48] comparison with them is hampered by the different methods/functionals used.

EXPERIMENTAL RESULTS

Table 1 shows the results of our synthesis study. The striking result is that the inverse-perovskite-type R_3MO including Mg was not obtained, although the other samples were almost single phase with minor extra phases. As shown in the Supporting Information (see Figure S-1), the sample with the nominal composition as Mg:Si:O = 3:1:1 was found to be a mixture with no trace of an inverse-perovskite-type structure. We examined the synthesis of $(R^{I},R^{II})_3MO$ solid solutions with

Table 1. Nominal Precursor Composition and the Obtained Compounds Identified by X-ray Diffraction

nominal precursor composition ratio					reaction products	
M		*R*				
Ge	Si	Mg	Ca	Sr	major phase	minor phases
1.0	0.0	0.0	3.0	0.0	Ca_3GeO	CaO, Ca_2Ge
0.0	1.0	0.0	3.0	0.0	Ca_3SiO	CaO, Ca_2Si
0.0	1.0	0.0	0.0	3.0	Sr_3SiO	SrO, Sr_2Si
0.5	0.5	0.0	1.0	0.0	$Ca_3(Si,Ge)O$	CaO, $Ca_2(Si,Ge)$
0.0	1.0	1.5	1.5	0.0	Ca_3SiO	Mg_2Si, MgO, $CaMg_2$, Ca_2Si, CaO, Ca
0.0	1.0	3.0	0.0	0.0	Mg_2Si, MgO	

R^1 = Mg, but there was no evidence for formation of $(Mg,R^{II})_3MO$ solid solutions. Indeed, the samples with the nominal composition as Mg:Ca:Si:O = 1.5:1.5:1:1 were a mixture containing Ca_3SiO, but the lattice parameters of the Ca_3SiO phase were exactly the same as those of the sample with the nominal composition Ca:Si:O = 3:1:1. The latter means that Mg cannot be dissolved into the oxysilicide or oxygermanide compounds with an inverse-perovskite-type structure due to the material's instability. We are not aware of published reports on stable Mg_3MO compounds with an inverse-perovskite-type phase, which is an important indication when considering the chemical bonding nature in R_3MO compounds.

To justify our results that $(Mg,R^{II})_3MO$ solid solutions could not be formed, we discuss the variation of the lattice parameters. As shown in Table 2, the lattice parameters of R_3MO compounds are very sensitive to substitution of *R* elements. Indeed, unit cell volumes of Ca_3SiO and Sr_3SiO differ significantly at 0.4192 and 0.5104 pm^3, respectively. On the other hand, lattice parameters of R_3MO are much less sensitive to substitution of *M* element. The unit cell volume of Ca_3GeO is 0.4225 pm^3, which is only by 0.8% larger than that of Ca_3SiO. As the lattice parameters are highly sensitive to substitution of *R* element, we can assume that incorporation of Mg into the R_3MO lattice should result in obvious reduction of lattice parameters in terms of ionic radius.[49,50] The lattice parameters of R_3MO will be discussed below in greater detail.

Further optical characterization was performed only for the Mg-free samples. The results of optical absorption measurements are shown in Figure 1. Here, the diffuse reflectance was converted into absorption. The observed absorbance spectra were converted into the Tauc plot shown in the inset of Figure 1. Optical band gap energy (E_g^o) was estimated by assuming a relationship:

$$(h\nu\alpha)^2 = K(h\nu - E_g^o) \tag{2}$$

Table 2. Experimentally Determined or Theoretically Calculated Lattice Parameters and Electronic Characteristics of R_3MO[a]

composition				lattice parameters			
R	*M*	fomula	method/functional	*a*/pm	*b*/pm	*c*/pm	characteristics
Mg	Si	Mg_3SiO	exptl		not obtained		N/A
			PBE	0.596	0.851	0.596	metallic
			PBEsol	0.592	0.844	0.592	metallic
			PBE0	0.591	0.843	0.591	metallic
			PBEsol0	0.588	0.839	0.588	metallic
Ca	Si	Ca_3SiO	exptl	0.667	0.943	0.667	E_g = 0.87 (eV)
			exptl [ref][b]	0.668	0.943	0.667	N/A
			PBE	0.668	0.946	0.669	E_g = 0.21 (eV)
			PBEsol	0.659	0.934	0.661	metallic
			PBE0	0.665	0.942	0.667	E_g = 1.22 (eV)
			PBEsol0	0.660	0.934	0.661	E_g = 1.07 (eV)
Ca	Si/Ge	$Ca_3(Si_{0.5}Ge_{0.5})O$	exptl	0.668	0.944	0.668	E_g = 0.84 (eV)
Ca	Ge	Ca_3GeO	exptl	0.669	0.945	0.669	E_g = 0.80 (eV)
			exptl [ref][b]	0.668	0.945	0.669	N/A
			PBE	0.670	0.948	0.673	E_g = 0.15 (eV)
			PBEsol	0.661	0.935	0.663	E_g = 0.05 (eV)
			PBE0	0.667	0.944	0.670	E_g = 1.23 (eV)
			PBEsol0	0.661	0.935	0.663	E_g = 1.14 (eV)
Sr	Si	Sr_3SiO	exptl	0.712	1.007	0.712	E_g = 0.84 (eV)
			exptl [ref][b]	0.713	1.007	0.712	N/A
			PBE	0.721	1.015	0.715	N/A
			PBEsol	0.708	1.001	0.706	0.24
			PBE0	0.715	1.009	0.712	1.41
			PBEsol0	0.707	1.000	0.705	1.26
Sr	Ge	Sr_3GeO	exptl [ref][b]	0.715	1.010	0.713	N/A
			PBE	0.723	1.019	0.718	E_g = 0.43 (eV)
			PBEsol	0.710	1.003	0.708	E_g = 0.29 (eV)
			PBE0	0.716	1.012	0.715	E_g = 1.36 (eV)
			PBEsol0	0.708	1.001	0.707	E_g = 1.27 (eV)

[a] The E_g values shown here were experimentally determined by diffuse reflectance measurement or by DFT calculations with various functionals.
[b] [ref]: ref 30.

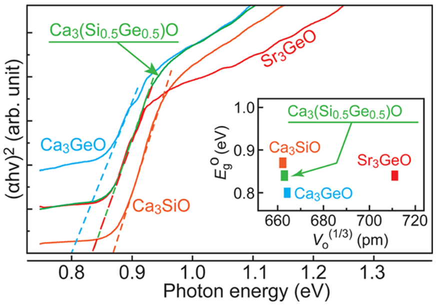

Figure 1. Optical absorption spectra of R_3MO samples. The inset shows the relationship between the cube root of unit cell volume ($V_0^{1/3}$) and optical energy band gap (E_g^o) determined from the absorption spectra.

Here, h is the Planck's constant, ν is frequency, α is absorption coefficient, and K is a constant, and a direct-transition-type energy band gap is assumed. On this assumption, E_g^o was estimated from the intercept in Figure 1. We note that the synthesized $Ca_3(Si_{0.5}Ge_{0.5})O$ compound has a band gap energy between that of Ca_3SiO and Ca_3GeO, indicating that Vegard's law works in this system. On the other hand, an interesting feature found in R_3MO compounds prepared in this study was that E_g^o did not significantly change with chemical composition. It seems that the compounds including heavier elements possess a slightly narrower E_g^o, but variation was very small. That also means that E_g^o is not significantly sensitive to changes in lattice parameters, as summarized in the inset of Figure 1. In fact, the lattice parameter of Sr_3SiO is larger but its E_g^o is almost the same as that of $Ca_3(Si_{0.5}Ge_{0.5})O$.

Figure 2 compares the luminescence and absorption spectra of Ca_3SiO at room temperature. It can be clearly seen that the luminescence peak and the absorption edge energies are very close, indicating that the Stokes shift between the absorption and emission peaks is negligibly small. More importantly, this is an experimental evidence that Ca_3SiO has a direct band gap. At the present stage, we have not evaluated the quantum efficiency of this luminescence, but it is important to note that the luminescence peak was observed even from the as-grown powder made by a very conventional solid-state reaction method.

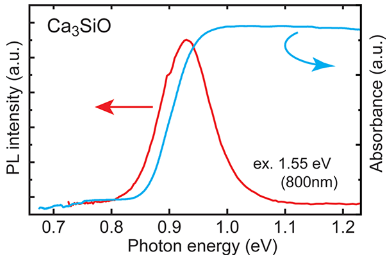

Figure 2. Luminescence spectrum and optical absorbance spectrum of Ca_3SiO measured at room temperature.

RESULTS OF CALCULATIONS

The synthesized Ca_3SiO and other R_3MO compounds exhibited semiconducting properties, e.g., band-edge luminescence, which originated in an optical band gap in the range of 0.8−0.9 eV. The PBE and PBEsol functionals indicate, however, that R_3MO compounds either have very small band gaps or exhibit metallic behavior. Using hybrid functionals often helps to reduce the self-interaction error, giving a better representation of the electronic structure and band gaps. The band structures of several compounds calculated using the nonlocal PBEsol0 functional are shown in Figure 3. The results confirm that R_3MO compounds have a direct band gap having both a valence band maximum (VBM) and conduction band minimum (CBM) at the Γ-point. The band diagrams of all four compounds calculated using the PBE0 functional are very similar, as shown in Figure 3. Therefore, the discussion below is mainly focused on the results of calculations using hybrid functionals.

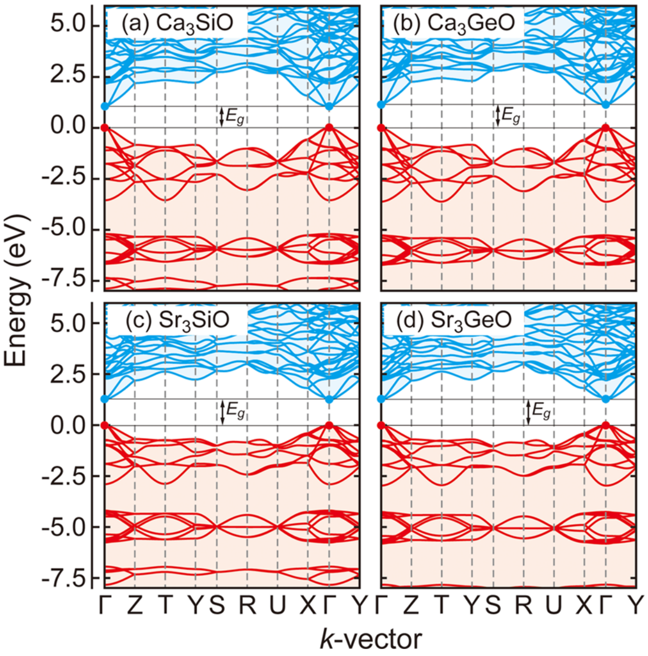

Figure 3. Electron band structures of some R_3MO (R = Ca, Sr; M = Si, Ge) compounds calculated with the PBEsol0 functional. Red and blue hatches indicate occupied and unoccupied states. The valence band maximum (VBM) and conduction band minimum (CBM) are indicated with red and blue dots, respectively, and lines and arrows indicate energy band gap (E_g), which is the energy difference between blue and red dots.

We use the enthalpy of formation as a measure of the compound's stability. Enthalpies (ΔH) were calculated using total energies of the following reaction

$$RO + Si + 2R \rightarrow R_3SiO \quad (R = Mg, Ca, Sr) \tag{3}$$

where positive (negative) values indicate an endothermic (exothermic) reaction, i.e., thermodynamically unstable (stable). As in experiment, calculations predict the Mg_3SiO to be unstable, with ΔH = 0.42 and 0.34 eV for the PBE and the PBEsol functionals. This confirms the experimentally observed instability of Mg-rich materials, which is corroborated further below. In contrast, the formation of Ca_3MO is spontaneous with ΔH = −1.43 eV for the PBE and −1.58 eV for the PBEsol functionals.

Table 2 summarizes the structural properties and the band gaps calculated with the local and nonlocal functionals of the synthesized inverse-perovskite-type materials. Comparison with the experimental data from previous and current studies is also shown. The calculated PBE lattice parameters are slightly larger than the PBEsol ones. There is no significant

https://dx.doi.org/10.1021/acs.inorgchem.0c02897

Table 3. Effective Mass of Electron and Hole in R_3MO Compounds Estimated from the Results of DFT Calculations[a]

		hole effective mass			electron effective mass		
compound	functional	Γ−Z	Γ−X	Γ−Y	Γ−Z	Γ−X	Γ−Y
Ca_3GeO	PBE0	−0.431	−0.815	−0.412	0.344	0.757	0.332
	PBEsol0	−0.348	−0.773	−0.342	0.335	0.741	0.323
Ca_3SiO	PBE0	−0.369	−0.965	−0.370	Γ_1: 0.401 Γ_2: 0.197	Γ_1: 0.751 Γ_2: 0.164	Γ_1: 0.385 Γ_2: 0.200
	PBEsol0	−0.323	−0.805	−0.337	0.356	0.742	0.347
Sr_3GeO	PBE0	−1.251	−2.635	−1.061	0.563	0.268	0.466
	PBEsol0	−0.849	−2.321	−0.604	0.537	0.263	0.447
Sr_3SiO	PBE0	−1.588	−2.441	−1.244	0.574	0.285	0.473
	PBEsol0	−0.763	−2.559	−0.625	0.540	0.268	0.452
Ca_3SnO	PBE0	Γ_1: −0.155 Γ_2: −0.488	Γ_1: −0.640 Γ_2: −0.645	Γ_1: −0.155 Γ_2: −0.488	0.274	0.731	0.274
	PBEsol0	Γ_1: −0.148 Γ_2: −0.464	Γ_1: −0.591 Γ_2: −0.591	Γ_1: −0.148 Γ_2: −0.464	0.271	0.731	0.271

[a] Notation of symmetry points in momentum space are as Γ for [0.00, 0.00, 0.00], Z for [0.00, 0.00, 0.50], X for [0.00, 0.50, 0.00], and Y for [−0.50, 0.00, 0.00], and two values, Γ_1 and Γ_2, are shown when electron bands are degenerated at the Γ-point.

variation of the lattice parameters calculated using the nonlocal functionals. The simulated and measured lattice parameters increase with the increase of the atomic number of the R element. This is because there is a positive correlation between the ionic radius of the R element and the atomic number.[49,50] For instance, the lattice parameters of Sr_3GeO are larger than those of Ca_3GeO. The lattice parameters are less affected by the substitution of the M elements than the R elements. For example, the unit cell volume of Sr_3SiO is much larger than that of Ca_3SiO but Ca_3SiO and Ca_3GeO volumes are nearly the same, although the atomic radius of Si is smaller than that of Ge. Variation of the lattice parameters in this manner are in good agreement with the experimental observations presented in Table 2. Hence, we can conclude that DFT simulations reproduce well the structural properties of R_3MO compounds.

The band gap energies calculated using nonlocal functionals are larger than those observed experimentally. We note that we are comparing the difference in the Kohn−Sham energies of the lowest unoccupied molecular orbital and the highest occupied molecular orbital with the optical adsorption spectra. There is no clear correlation between E_g^o and the chemical composition. As suggested by our h-DFT calculations, the effect on the band gap energy is stronger for the substitution of R element than that of M element; e.g., the band gap increased by 0.1−0.2 eV with Sr substituting Ca, while it decreased by less than 0.1 eV when Ge substitutes Si. We think this trend should be general in R_3MO systems. A correlation between the band gap energy and the lattice parameters is discussed below.

The amount of experimental information on the electronic transport properties of our powder materials is limited. We can, however, calculate the effective electron and hole masses from the band structure using eq 1. In general, materials show relatively small electron and hole effective masses (see Table 3), which are favorable properties for electronic applications. Our calculations suggest heavier effective masses for electrons and holes in R = Sr compared to R = Ca compounds. The chemical composition effect is discussed in detail in the following section.

The results of Bader analysis of ionic charges are summarized in Table 4. They demonstrate that R_3MO are highly ionic crystals. The values for R and O shown in Table 4 are close to those in oxides characterized by their ionic bonding, e.g., +1.69e for Mg in MgO,[51] +1.56e for Ca in $CaTiO_3$,[52] +1.61e for Sr in $SrTiO_3$,[52] +1.7e for Ba in $Ba_2TiSi_2O_8$,[53] and +1.7e for Ba in $BaTiO_3$.[53] Consequently, effective charges of M elements have to be negative and large for compensation. We note that the Bader charge of Si in silicates is close to +2.3e, whereas its formal charge is +4e.[53] However, M elements in R_3MO are unquestionably *anions* with negative effective charges exceeding −2.4e. It is also interesting to note that effective charges of Sr and Ca shown in Table 4 are close to each other regardless of M and that effective charges of Si and Ge are almost the same regardless of R. This may be the reason for very similar band structures of R_3MO (R = Sr, Ca, and M = Si, Ga). On the other hand, the Mg and Si Bader charges in Mg_3SiO are clearly different from those of the other compounds. This is a good indication that chemical bonds involving Mg in R_3MO are quite different from those involving Ca and Sr in R_3MO. This peculiar behavior of Mg correlates with the instability of Mg_3MO.

Table 4. Results of Bader Charges Analysis for R_3MO and R_2M (R = Mg, Ca, or Sr; M = Si or Ge) Compounds

	element/charge (e)		
compound	R	M	O
Ca_3SiO	Ca/1.35	Si/−2.50	−1.54
Ca_3GeO	Ca/1.32	Ge/−2.40	−1.55
Sr_3SiO	Sr/1.32	Si/−2.40	−1.55
Sr_3GeO	Sr/1.32	Ge/−2.40	−1.55
Mg_3SiO	Mg/1.32	Si/−2.40	−1.55
Ca_2Si	Ca/1.25	Si/−2.57	
Ca_2Ge	Ca/1.25	Ge/−2.56	
Sr_2Si	Sr/1.19	Si/−2.44	
Sr_2Ge	Sr/1.18	Ge/−2.43	
Mg_2Ge[a]	Mg/1.2	Ge/−2.65	
Mg_2Si[a]	Mg/1.50	Si/−3.00	

[a] Fluorite-type structure.

■ DISCUSSION

Measured and calculated structural parameters of R_3MO suggest that the lattice parameters of these compounds are governed by the R−O bond length. The calculated R−O distances are 255 pm for Sr_3MO and 236−237 pm for Ca_3MO, which are in close agreement with those measured by single crystal X-ray diffraction.[29,30] It has to be noted that these values are very close to the *R*−O distances in SrO and CaO with a rock-salt structure,[54] suggesting that the *R*−O bonds in R_3MO compounds are very similar to those in typical oxides. This implies that the *M* elements have to be anions to compensate the positive charge of the *R* elements, which is also demonstrated by the Bader population analysis discussed above. On the other hand, the lattice parameters of the R_3MO compounds are not sensitive to substitution of *M* elements. The interatomic distances in Si and Ge in the diamond structure are within about 235 and 246 pm, and their band gap energies are 1.1 and 0.67 eV, respectively. In contrast, the *M*−*M* interatomic distances change only with substitution of the *R* element and *M*−*M* distances are not sensitive to substitution of *M* element. For example, the Si−Si and Ge−Ge distances in Sr_3SiO and Sr_3GeO differ only by 2 pm. Hence, we can conclude that the lattice parameters of the R_3MO materials are determined by the *R*−O bond length.

This consideration is supported by the local density of states (LDOS). Figure 4 shows the results of LDOS analysis for Sr_3SiO calculated using the PBEsol0 functional. Additional results of LDOS calculations are shown in Figure S-2 in the Supporting Information. Here, O-*p* electronic states are found to be about 4−7 eV below the valence band maximum (VBM), whereas the conduction band minimum (CBM) is composed of *d* states of the *R* elements. Thus, the O-2*p* oxygen states (O-*p* in Figure 4) form a *deeper* valence band. On the other hand, the top of the valence band at 0−3.5 eV is dominated by *p* states of *M* elements. This implies that the electronic structure of R_3MO compounds can be viewed as a *superposition* of electronic structures attributed to the R_2M component, having a narrow band gap, and that of *RO* with a wider band gap, and the resulting band gap of R_3MO is determined by that of the R_2M component. The energy band gap of CaO was experimentally determined to be 7.1 eV[55] and calculated to be 6.6 eV within the GW approximation;[56] for SrO, it is approximately 6 eV from observed reflection spectra,[57] and 7.24 eV within the GW approximation.[58] The energy differences between CBM and the top edge of O-2*p* bands calculated for R_3MO compounds are very similar, as shown in Figures 4 and S-2. The dispersion of electron energy in momentum space does not seem to change by elemental substitution either (see Figure 3). There is no difference between Sr_3GeO and Sr_3SiO band structures to the naked eye.

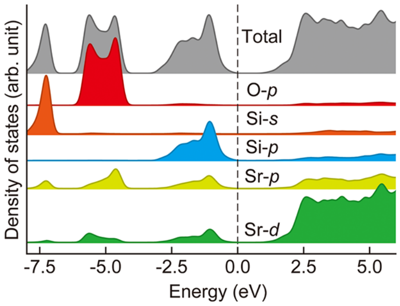

Figure 4. Local density of states (LDOS) for Sr_3SiO calculated using the PBEsol0 functional. The vertical scale is in arbitrary unit for visibility.

The geometric and electronic structures of R_3MO compounds demonstrate that these are ionic crystals where *M* elements serve as anions with −4*e* formal charge, but the band dispersion of *M* elements is very similar to that for Si and Ge. Analysis of the R_2M electronic structure supports our assertion that the electronic structure of R_3MO can be viewed as that of the R_2M component with a narrow band gap being superimposed onto that of the *RO* component with a wider band gap and that substitution of *M* elements does not affect electronic structures because of the strong ionic characteristics of M^{4-} anions. Figure 5 shows DOS for Ca_2Ge,[59] Ca_2Si,[59] Mg_2Si ($Fm3m$),[60] Mg_2Ge ($Fm3m$),[61] Sr_2Si,[62] and Sr_2Ge[63] compounds calculated using the PBEsol0 functional. As seen in the top and middle panels, the Ge/Si substitution has a minor effect on the DOS. In addition, the main features of the DOS profile of the compounds with *R* = Ca are very similar to those with *R* = Sr. The effect of elemental substitution shown here is very similar to that shown in Figure 3 and Figure S-2 in the Supporting Information. It seems that M^{4-} anions behave like point charges and their contribution to the band dispersion and band gap is minor compared to that of the Madelung potential. This idea is also supported by comparing the results of Bader population analysis for R_3MO and R_2M shown in Table 4. The effective charges of *R* and *M* in those compounds are very similar to each other, demonstrating that both R_3MO and R_2M are highly ionic crystals. The fact that the band structures of R_3MO and R_2M do not change with *R* and *M* substitution is likely a cause for the very small change of the R_3MO energy band gap by *M* element substitution seen in Figure 1 and Table 2.

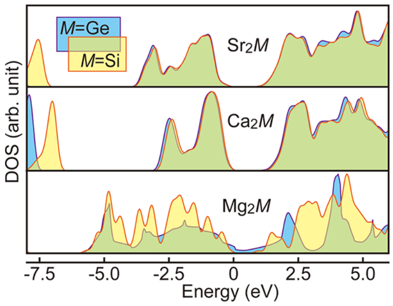

Figure 5. Density of states (DOS) for some R_2M compounds (*R* = Mg, Ca, or Sr; *M* = Si or Ge) calculated by using the PBEsol0 functional. Calculations for Mg_2M were performed for one of the reported polymorphs, the fluorite-type structure.

We note that the electronic structure of Mg_2M compounds with a fluorite structure (bottom panel in Figure 5) is different from that of other R_2M compounds studied here. Indeed, the DOS dispersion for Mg_2Si is clearly different from those for the other two compounds. The most critical difference between Mg and other *R* elements is in the lowest excited states. The excited orbital of Mg is 3*p* states, while, for Sr and Ca, these are 4*d* and 3*d* states, respectively. This may be the reason for the difference between Mg_2M and other R_2M electronic structures. Further band gap tuning of R_3MO could be achieved by substituting Mg for Ca to make the lattice parameter smaller. Unfortunately, as shown above, Mg does not dissolve in the R_3MO lattice. The most obvious difference between Mg and the other alkali earth elements is that Mg is on the third row in the periodic table and there is a lack of *d* orbitals, while the first excited states of Ca and Sr are 3*d* and 4*d* orbitals, respectively. This suggests that the contribution of *d* orbitals to chemical bonding is essential for the stability of R_3MO compounds with an inverse-perovskite-type structure. Since *R*−O bonds in R_3MO and rock-salt compounds are very similar, we can draw an analogy between the nature of the R−O bonds in R_3MO and MO compounds. In this context, we refer to the phase diagram of the MgO−CaO pseudo-binary system.[64,65] It is evident that solubility of CaO in MgO or MgO in CaO is very narrow and the wide miscibility gap opens up in this pseudo-binary system. This MgO−CaO miscibility indicates that formation of $(Ca,Mg)_3MO$ should be very difficult. On the other hand, the pseudo-binary CaO−SrO phase diagram has a wide solid solution range at relatively low temperature.[66] The large miscibility gap between MgO and CaO has been attributed to the absence of *d* orbitals in Mg. Therefore, tuning of semiconductor lattice parameters via adjusting R−O chemical bonds by elemental substitution using Mg is very difficult.

Finally, we briefly discuss the band alignment of R_3MO compounds. Since the electronic structure of R_3MO possesses characteristics of both RO and R_2M, one can use the band diagram of the R_2M and RO compounds to align them with the corresponding R_3MO energy states and, thus, estimate their ionization potential and electron affinity. The experimental bulk ionization potential of CaO and SrO is 6.25 and 5.30 eV, which is in good agreement with those calculated with highly accurate DFT calculations using hybrid functionals.[67,68] Note that the ionization potential for those typical oxides is calculated using the VBM energy, which is mainly composed of the O-2*p* band, with respect to the vacuum level. Hence, the ionization energy of the R_3MO compounds was estimated by aligning the top of the O-2*p* band in R_3MO to the ionization potential of CaO and SrO, as shown in Figure 6. The calculated top of the O-2*p* band in R_3MO is about 5.0 eV below VBM for R = Ca and 4.1 eV for R = Sr (see Figures 3, 4, and S-2). Therefore, the ionization potential for R_3MO (R = Ca or Sr) compounds is estimated to be around 1.20−1.25 eV. This value is relatively small, which encourages us to work on doping through hole injection. Moreover, these materials are expected to show good catalytic properties. We note that analysis of the R_3MO refractive indexes is beyond the scope of the current work. This is, however, needed to construct optical devices based on these materials. Further investigation of R_3MO solid solutions is in progress and will be reported in a separate publication.

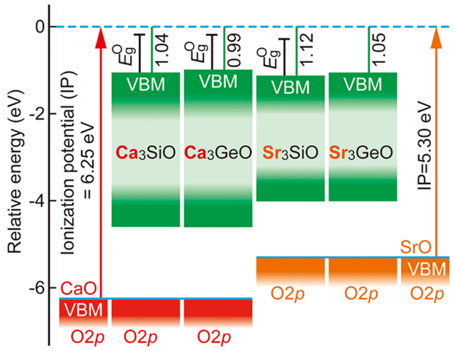

Figure 6. Estimation of ionization potential for R_3MO (R = Ca or Sr; M = Si or Ge) by aligning calculated high energy ends of the O-2*p* band to the valence band maximum (VBM) of known RO compounds. Vacuum level is set to zero in energy scale, and the lengths of the bar denoted by E_g^o indicate experimentally determined energy band gap.

■ CONCLUSIONS

We have synthesized inverse-perovskite-type oxysilicides and oxygermanides, R_3MO (R = Ca, Sr; M = Si, Ge), and investigated their optical properties. The materials are semiconductors with a direct optical band gap, as suggested by their optical absorption edges and luminescence spectra. These findings were corroborated by hybrid DFT calculations, where a direct band gap was calculated from their band structures. Band gaps are determined to be 0.8−0.9 eV, with no significant change upon elemental substitution. This feature is driven by their structural properties, in particular, the M−M bond distances. It is also shown that incorporation of Mg into the R_3MO lattice is energetically unfavorable. That is a limitation for optoelectronic device applications of R_3MO compounds since band gap engineering is limited. In contrast, relatively small ionization potentials of R_3MO compounds are estimated, which is another interesting feature for practical applications.

To summarize, we have synthesized a new class of materials with potential applications as semiconductors in IR devices. These materials are made from earth abundant and nontoxic elements, with a relatively light electron/hole effective mass and a direct band gap. Our findings represent, therefore, a big step into the design of new nontoxic materials with high functionality.

■ ASSOCIATED CONTENT

Supporting Information

The Supporting Information is available free of charge at https://pubs.acs.org/doi/10.1021/acs.inorgchem.0c02897.

S-1: X-ray diffraction. Phase identification and structural analysis for R_3MO compounds. S-2: Density of states for every different compositions. Local DOS for R_3MO compounds not displayed in the text (PDF)

■ AUTHOR INFORMATION

Corresponding Author

Naoki Ohashi − *National Institute for Materials Science (NIMS), Tsukuba, Ibaraki 305-0044, Japan; Materials Center for Elemental Strategy (MCES), Tokyo Institute of Technology (Tokyo Tech), Yokohama 226-8503, Japan;* orcid.org/0000-0002-4011-0031; Email: OHASHI.Naoki@nims.go.jp

Authors

David Mora-Fonz − *Department of Physics and Astronomy, University College London, London WC1E 6BT, United Kingdom;* orcid.org/0000-0002-0310-9891
Shigeki Otani − *National Institute for Materials Science (NIMS), Tsukuba, Ibaraki 305-0044, Japan*
Takeshi Ohgaki − *National Institute for Materials Science (NIMS), Tsukuba, Ibaraki 305-0044, Japan*
Masashi Miyakawa − *National Institute for Materials Science (NIMS), Tsukuba, Ibaraki 305-0044, Japan*
Alexander Shluger − *Department of Physics and Astronomy, University College London, London WC1E 6BT, United Kingdom*

Complete contact information is available at: https://pubs.acs.org/10.1021/acs.inorgchem.0c02897

Notes

The authors declare no competing financial interest.

■ ACKNOWLEDGMENTS

This study was partly supported by the MEXT Element Strategy Initiative to Form Core Research Center (Grant Number JPMXP0112101001). We are grateful to JSPS and EPSRC for support under the core-to-core scheme, project "Defect Functionalized Sustainable Energy Materials: From Design to Devices Application" (EPSRC grant EP/R034540/1). We also acknowledge funding provided by EPSRC under grant EP/P013503/1 and by JSPS grant #JPJSCCA20180006. Via our membership of the UK's HEC Materials Chemistry Consortium, which is funded by EPSRC (EP/L000202); this work used the UK Materials and Molecular Modelling Hub for computational resources, MMM Hub, which is partially funded by EPSRC (EP/P020194).

■ REFERENCES

(1) Koyama, F. Recent Advances of VCSEL Photonics. *J. Lightwave Technol.* **2006**, *24* (12), 4502−4513.

(2) Campbell, J. C.; Demiguel, S.; Ma, F.; Beck, A.; Guo, X.; Wang, S.; Zheng, X.; Li, X.; Beck, J. D.; Kinch, M. A.; Huntington, A.; Coldren, L. A.; Decobert, J.; Tscherptner, N. Recent Advances in Avalanche Photodiodes. *IEEE J. Sel. Top. Quantum Electron.* **2004**, *10* (4), 777−787.

(3) Rogalski, A.; Antoszewski, J.; Faraone, L. Third-Generation Infrared Photodetector Arrays. *J. Appl. Phys.* **2009**, *105* (9), 091101.

(4) Rogalski, A. Infrared Detectors: Status and Trends. *Prog. Quantum Electron.* **2003**, *27* (2−3), 59−210.

(5) Boening, D. W. Ecological Effects, Transport, and Fate of Mercury: A General Review. *Chemosphere* **2000**, *40* (12), 1335−1351.

(6) Järup, L.; Åkesson, A. Current Status of Cadmium as an Environmental Health Problem. *Toxicol. Appl. Pharmacol.* **2009**, *238* (3), 201−208.

(7) Stohs, S. Oxidative Mechanisms in the Toxicity of Metal Ions. *Free Radical Biol. Med.* **1995**, *18* (2), 321−336.

(8) Taylor, A. Biochemistry of Tellurium. *Biol. Trace Elem. Res.* **1996**, *55* (3), 231−239.

(9) Johnson, J. L.; Samoska, L. A.; Gossard, A. C.; Merz, J. L.; Jack, M. D.; Chapman, G. R.; Baumgratz, B. A.; Kosai, K.; Johnson, S. M. Electrical and Optical Properties of Infrared Photodiodes Using the InAs/Ga$_{1-x}$In$_x$Sb Superlattice in Heterojunctions with GaSb. *J. Appl. Phys.* **1996**, *80* (2), 1116−1127.

(10) Jeon, H.; Ding, J.; Nurmikko, A. V.; Xie, W.; Grillo, D. C.; Kobayashi, M.; Gunshor, R. L.; Hua, G. C.; Otsuka, N. Blue and Green Diode Lasers in ZnSe-based Quantum Wells. *Appl. Phys. Lett.* **1992**, *60* (17), 2045−2047.

(11) Butte, R; Carlin, J-F; Feltin, E; Gonschorek, M; Nicolay, S; Christmann, G; Simeonov, D; Castiglia, A; Dorsaz, J; Buehlmann, H J; Christopoulos, S; Baldassarri Hoger von Hog, G; Grundy, A J D; Mosca, M; Pinquier, C; Py, M A; Demangeot, F; Frandon, J; Lagoudakis, P G; Baumberg, J J; Grandjean, N Current Status of AlInN Layers Lattice-Matched to GaN for Photonics and Electronics. *J. Phys. D: Appl. Phys.* **2007**, *40* (20), 6328−6344.

(12) Kondow, M.; Kitatani, T.; Nakatsuka, S.; Larson, M. C.; Nakahara, K.; Yazawa, Y.; Okai, M.; Uomi, K. GaInNAs: A Novel Material for Long-Wavelength Semiconductor Lasers. *IEEE J. Sel. Top. Quantum Electron.* **1997**, *3* (3), 719−730.

(13) Zhang, S. B.; Wei, S.-H.; Zunger, A.; Katayama-Yoshida, H. Defect Physics of the CuInSe$_2$ Chalcopyrite Semiconductor. *Phys. Rev. B: Condens. Matter Mater. Phys.* **1998**, *57* (16), 9642−9656.

(14) Persson, C.; Zhao, Y.-J.; Lany, S.; Zunger, A. *N*-Type Doping of CuInSe$_2$ and CuGaSe$_2$. *Phys. Rev. B: Condens. Matter Mater. Phys.* **2005**, *72* (3), 035211.

(15) Jackson, P.; Wuerz, R.; Hariskos, D.; Lotter, E.; Witte, W.; Powalla, M. Effects of Heavy Alkali Elements in Cu(In,Ga)Se2 Solar Cells with Efficiencies up to 22.6%. *Phys. Status Solidi RRL* **2016**, *10* (8), 583−586.

(16) Morris, R. G.; Redin, R. D.; Danielson, G. C. Semiconducting Properties of Mg$_2$Si Single Crystals. *Phys. Rev.* **1958**, *109* (6), 1909−1915.

(17) Hao, J. H.; Guo, Z. G.; Jin, Q. H. First Principles Calculation of Structural Phase Transformation in Mg$_2$Si at High Pressure. *Solid State Commun.* **2010**, *150* (47−48), 2299−2302.

(18) El-Amir, A. A. M.; Ohsawa, T.; Ishii, S.; Imura, M.; Liao, M.; Fu, X.; Segawa, H.; Sakaguchi, I.; Nagao, T.; Shimamura, K.; Ohashi, N. Silicon-Compatible Mg$_2$Si/Si *n-p* Photodiodes with High Room Temperature Infrared Responsivity. *Mater. Sci. Semicond. Process.* **2019**, *102* (June), 104577.

(19) Akasaka, M.; Iida, T.; Matsumoto, A.; Yamanaka, K.; Takanashi, Y.; Imai, T.; Hamada, N. The Thermoelectric Properties of Bulk Crystalline *n*- and *p*-Type Mg$_2$Si Prepared by the Vertical Bridgman Method. *J. Appl. Phys.* **2008**, *104* (1), 013703.

(20) Stella, A.; Lynch, D. W. Photoconductivity in Mg$_2$Si and Mg$_2$Ge. *J. Phys. Chem. Solids* **1964**, *25* (11), 1253−1259.

(21) Janka, O.; Zaikina, J. V.; Bux, S. K.; Tabatabaifar, H.; Yang, H.; Browning, N. D.; Kauzlarich, S. M. Microstructure Investigations of Yb- and Bi-Doped Mg$_2$Si Prepared from Metal Hydrides for Thermoelectric Applications. *J. Solid State Chem.* **2017**, *245*, 152−159.

(22) Mahan, J. E.; Vantomme, A.; Langouche, G.; Becker, J. P. Semiconducting Mg2Si Thin Films Prepared by Molecular-Beam Epitaxy. *Phys. Rev. B: Condens. Matter Mater. Phys.* **1996**, *54* (23), 16965−16971.

(23) Baranek, P.; Schamps, J. Influence of Electronic Correlation on Structural, Dynamic, and Elastic Properties of Mg2Si. *J. Phys. Chem. B* **1999**, *103* (14), 2601−2606.

(24) Imai, Y.; Watanabe, A.; Mukaida, M. Electronic Structures of Semiconducting Alkaline-Earth Metal Silicides. *J. Alloys Compd.* **2003**, *358* (1−2), 257−263.

(25) Miyazaki, H. T. Unconventional Thermal Emission from Photonic Crystals. In *Micro- and Nanophotonic Technologies*; Meyrueis, P., Van de Voorde, M., Sakoda, K., Eds.; Wiley-VCH Verlag GmbH & Co. KGaA: Weinheim, Germany, 2017; pp 51−64. DOI: 10.1002/9783527699940.ch3.

(26) Miyazaki, H. T.; Mano, T.; Kasaya, T.; Osato, H.; Watanabe, K.; Sugimoto, Y.; Kawazu, T.; Arai, Y.; Shigetou, A.; Ochiai, T.; Jimba, Y.; Miyazaki, H. Synchronously Wired Infrared Antennas for Resonant Single-Quantum-Well Photodetection up to Room Temperature. *Nat. Commun.* **2020**, *11* (1), 565.

(27) Pöhls, J.-H.; Mar, A. Thermoelectric Properties of Inverse Perovskites A_3TtO (A = Mg, Ca; Tt = Si, Ge): Computational and Experimental Investigations. *J. Appl. Phys.* **2019**, *126* (2), 025110.

(28) Oudah, M.; Ikeda, A.; Hausmann, J. N.; Yonezawa, S.; Fukumoto, T.; Kobayashi, S.; Sato, M.; Maeno, Y. Superconductivity in the Antiperovskite Dirac-Metal Oxide Sr$_{3-x}$SnO. *Nat. Commun.* **2016**, *7* (1), 13617.

(29) Huang, B.; Corbett, J. D. Orthorhombic Inverse Perovskitic Ba$_3Tt$O (Tt = Ge, Si) as Zintl Phases. *Z. Anorg. Allg. Chem.* **1998**, *624* (11), 1787−1790.

(30) Velden, A.; Jansen, M. Zur Kenntnis Der Inversen Perowskite M_3TO (M = Ca, Sr, Yb; T = Si, Ge, Sn, Pb). *Z. Anorg. Allg. Chem.* **2004**, *630* (2), 234−238.

(31) Nuss, J.; Mühle, C.; Hayama, K.; Abdolazimi, V.; Takagi, H. Tilting Structures in Inverse Perovskites, M_3TtO (M = Ca, Sr, Ba, Eu; Tt = Si, Ge, Sn, Pb). *Acta Crystallogr., Sect. B: Struct. Sci., Cryst. Eng. Mater.* **2015**, *71* (3), 300−312.

(32) Kresse, G.; Hafner, J. Ab Initio Molecular-Dynamics Simulation of the Liquid-Metal−Amorphous-Semiconductor Transition in Germanium. *Phys. Rev. B: Condens. Matter Mater. Phys.* **1994**, *49* (20), 14251−14269.

(33) Kresse, G.; Furthmüller, J. Efficiency of Ab-Initio Total Energy Calculations for Metals and Semiconductors Using a Plane-Wave Basis Set. *Comput. Mater. Sci.* **1996**, *6* (1), 15−50.

(34) Blöchl, P. E. Projector Augmented-Wave Method. *Phys. Rev. B: Condens. Matter Mater. Phys.* **1994**, *50* (24), 17953−17979.

(35) Kresse, G.; Joubert, D. From Ultrasoft Pseudopotentials to the Projector Augmented-Wave Method. *Phys. Rev. B: Condens. Matter Mater. Phys.* **1999**, *59* (3), 1758−1775.

(36) Perdew, J. P.; Burke, K.; Ernzerhof, M. Generalized Gradient Approximation Made Simple. *Phys. Rev. Lett.* **1996**, *77* (18), 3865−3868.

(37) Perdew, J. P.; Ruzsinszky, A.; Csonka, G. I.; Vydrov, O. A.; Scuseria, G. E.; Constantin, L. A.; Zhou, X.; Burke, K. Restoring the Density-Gradient Expansion for Exchange in Solids and Surfaces. *Phys. Rev. Lett.* **2008**, *100* (13), 136406.

(38) Perdew, J. P.; Ernzerhof, M.; Burke, K. Rationale for Mixing Exact Exchange with Density Functional Approximations. *J. Chem. Phys.* **1996**, *105* (22), 9982−9985.

(39) Adamo, C.; Barone, V. Toward Reliable Density Functional Methods without Adjustable Parameters: The PBE0Model. *J. Chem. Phys.* **1999**, *110* (13), 6158−6170.

(40) *International Tables for Crystallography*, Vol. *A*; Hahn, T., Ed.; International Union of Crystallography: Chester, England, 2006. DOI: 10.1107/97809553602060000100.

(41) Monkhorst, H. J.; Pack, J. D. Special Points for Brillouin-Zone Integrations. *Phys. Rev. B* **1976**, *13* (12), 5188−5192.

(42) Pack, J. D.; Monkhorst, H. J. Special Points for Brillouin-Zone Integrations"—a Reply. *Phys. Rev. B* **1977**, *16* (4), 1748−1749.

(43) Ganose, A. M.; Jackson, A. J.; Scanlon, D. O. Sumo: Command-Line Tools for Plotting and Analysis of Periodic Ab Initio Calculations. *J. Open Source Softw.* **2018**, *3* (28), 717.

(44) Kutzelnigg, W. Atoms in Molecules. A Quantum Theory. (Reihe: International Series of Monographs on Chemistry, Vol. 22.) Von R.F.W. Bader. Clarendon Press, Oxford, 1990. XVIII, 438 S., geb. £ 50.00. − ISBN 0-19-855168-1. *Angew. Chem.* **1992**, *104* (10), 1423−1423.

(45) Ud Din, H.; Reshak, A. H.; Murtaza, G.; Amin, B.; Ali, R.; Alahmed, Z. A.; Chyský, J.; Bila, J.; Kamarudin, H. Structural, Elastic, Thermal and Electronic Properties of M_2X (M = Sr, Ba and X = Si, Ge, Sn) Compounds in Anti-Fluorite Structure: First Principle Calculations. *Indian J. Phys.* **2015**, *89* (4), 369−375.

(46) Lebègue, S.; Arnaud, B.; Alouani, M. Calculated Quasiparticle and Optical Properties of Orthorhombic and Cubic Ca_2Si. *Phys. Rev. B: Condens. Matter Mater. Phys.* **2005**, *72* (8), 085103.

(47) Migas, D. B.; Miglio, L.; Shaposhnikov, V. L.; Borisenko, V. E. Comparative Study of Structural, Electronic and Optical Properties of Ca_2Si. *Phys. Rev. B: Condens. Matter Mater. Phys.* **2003**, *67* (20), 205203.

(48) Migas, D. B.; Bogorodz, V. O.; Filonov, A. B.; Shaposhnikov, V. L.; Borisenko, V. E.; Galkin, N. G. Electronic Properties of Semiconducting Ca_2Si Silicide: From Bulk to Nanostructures by Means of First Principles Calculations. *Jpn. J. Appl. Phys.* **2015**, *54* (7S2), 07JA03.

(49) Shannon, R. D.; Prewitt, C. T. Effective Ionic Radii in Oxides and Fluorides. *Acta Crystallogr., Sect. B: Struct. Crystallogr. Cryst. Chem.* **1969**, *25* (5), 925−946.

(50) Shannon, R. D.; Prewitt, C. T. Revised Values of Effective Ionic Radii. *Acta Crystallogr., Sect. B: Struct. Crystallogr. Cryst. Chem.* **1970**, *26* (7), 1046−1048.

(51) Kosa, M.; Barad, H. N.; Singh, V.; Keller, D. A.; Shimanovich, K.; Rühle, S.; Anderson, A. Y.; Zaban, A.; Major, D. T. A Combined Computational and Experimental Investigation of Mg Doped α-Fe_2O_3. *Phys. Chem. Chem. Phys.* **2016**, *18* (2), 781−791.

(52) Beck, H. P. A DFT Study on the Correlation between Topology and Bader Charges: Part III, the Development of Charge, "Size" and Coordination in Alkali and Alkaline Earth Titanates(IV). *Solid State Sci.* **2015**, *48*, 61−71.

(53) Taylor, N. T.; Davies, F. H.; Hepplestone, S. P. First Principles Electronic and Elastic Properties of Fresnoite $Ba_2TiSi_2O_8$. *Mater. Res. Express* **2017**, *4* (12), 125904.

(54) Baltache, H.; Khenata, R.; Sahnoun, M.; Driz, M.; Abbar, B.; Bouhafs, B. Full Potential Calculation of Structural, Electronic and Elastic Properties of Alkaline Earth Oxides MgO, CaO and SrO. *Phys. B* **2004**, *344* (1−4), 334−342.

(55) Whited, R. C.; Flaten, C. J.; Walker, W. C. Exciton Thermoreflectance of MgO and CaO. *Solid State Commun.* **1973**, *13* (11), 1903−1905.

(56) Yamasaki, A.; Fujiwara, T. Electronic Structure of the *M*O Oxides (*M*=Mg, Ca, Ti, V) in the GW Approximation. *Phys. Rev. B: Condens. Matter Mater. Phys.* **2002**, *66* (24), 245108.

(57) Kaneko, Y.; Morimoto, K.; Koda, T. Optical Properties of Alkaline-Earth Chalcogenides. II. Vacuum Ultraviolet Reflection Spectra in the Synchrotron Radiation Region of 4−40 EV. *J. Phys. Soc. Jpn.* **1983**, *52* (12), 4385−4396.

(58) Cappellini, G.; Finocchi, F.; Bouette-Russo, S.; Noguera, C. Ground-State Properties and Excitation Energies of Cubic SrO and MgO. *Comput. Mater. Sci.* **2001**, *20* (3−4), 401−406.

(59) Eckerlin, P.; Wölfel, E. Die Kristallstruktur von Ca_2Si Und Ca_2Ge. *Z. Anorg. Allg. Chem.* **1955**, *280* (5−6), 321−331.

(60) Saravanan, R.; Robert, M. C. Local Structure of the Thermoelectric Material Mg_2Si Using XRD. *J. Alloys Compd.* **2009**, *479* (1−2), 26−31.

(61) Grosch, G. H.; Range, K.-J. Studies on AB_2-Type Intermetallic Compounds, I. Mg_2Ge and Mg_2Sn: Single-Crystal Structure Refinement and Ab Initio Calculations. *J. Alloys Compd.* **1996**, *235* (2), 250−255.

(62) Widera, A.; Eisenmann, B.; Schäfer, H. Notizen: Darstellung Und Kristallstruktur Des Sr_2Si. *Z. Naturforsch., B: J. Chem. Sci.* **1976**, *31* (4), 520−521.

(63) Eisenmann, B.; Schäfer, H.; Turban, K. Neue Intermetallische Verbindungen Im Anti-$PbCl_2$Typ. *Z. Naturforsch., B: J. Chem. Sci.* **1975**, *30* (9−10), 677−680.

(64) Walle, A.; Ceder, G. Automating First-Principles Phase Diagram Calculations. *J. Phase Equilib.* **2002**, *23* (4), 348−359.

(65) Yin, Y.; Argent, B. The Phase Diagrams and Thermodynamics of the ZrO_2-CaO-MgO and MgO-CaO Systems. *J. Phase Equilib.* **1993**, *14* (5), 588−600.

(66) Jacob, K. T.; Raj, P. M.; Waseda, Y. The CaO-SrO-CuO-O_2 System: Phase Equilibria and Thermodynamic Properties at 1123 K. *J. Phase Equilib.* **1995**, *16* (2), 113−120.

(67) Logsdail, A. J.; Scanlon, D. O.; Catlow, C. R. A.; Sokol, A. A. Bulk Ionization Potentials and Band Alignments from Three-Dimensional Periodic Calculations as Demonstrated on Rocksalt Oxides. *Phys. Rev. B: Condens. Matter Mater. Phys.* **2014**, *90* (15), 155106.

(68) Logsdail, A. J.; Mora-Fonz, D.; Scanlon, D. O.; Catlow, C. R. A.; Sokol, A. A. Structural, Energetic and Electronic Properties of (100) Surfaces for Alkaline Earth Metal Oxides as Calculated with Hybrid Density Functional Theory. *Surf. Sci.* **2015**, *642*, 58−65.